Local and global properties of energy transfer in models of plasma turbulence

Christian L Vásconez, D Perrone, R Marino, D Laveder, F Valentini, S Servidio, P Mininni, L Sorriso-Valvo

Local and global properties of energy transfer in models of plasma turbulence

Christian L. Vásconez [1,†], D. Perrone[2], R. Marino[3], D. Laveder[4], F. Valentini [5], S. Servidio[5], P. Mininni[6] and L. Sorriso-Valvo [7,8]

[1]Departamento de Física, Escuela Politécnica Nacional, Ladrón de Guevara E11-253, 170525 Quito, Ecuador

[2]ASI – Italian Space Agency, Via del Politecnico snc, 00133 Rome, Italy

[3]Laboratoire de Mécanique des Fluides et d'Acoustique, CNRS, École Centrale de Lyon, Université Claude Bernard Lyon 1, INSA de Lyon, Écully F-69134, France

[4]Université Côte d'Azur, CNRS, Observatoire de la Côte d'Azur, Laboratoire J. L. Lagrange, Boulevard de l'Observatoire, CS 34229, 06304 Nice CEDEX 4, France

[5]Dipartimento di Fisica, Università della Calabria, I-87036 Rende (CS), Italy

[6]Departamento de Física, Universidad de Buenos Aires and IFIBA, CONICET, 1428 Buenos Aires, Argentina

[7]Istituto per la Scienza e Tecnologia dei Plasmi (ISTP), Consiglio Nazionale delle Ricerche, Via Amendola 122/D, 70126 Bari, Italy

[8]Swedish Institute of Space Physics, Ångström Laboratory, Lägerhyddsvägen 1, SE-751 21 Uppsala, Sweden

The nature of the turbulent energy transfer rate is studied using direct numerical simulations of weakly collisional space plasmas. This is done comparing results obtained from hybrid Vlasov–Maxwell simulations of collisionless plasmas, Hall magnetohydrodynamics and Landau fluid models reproducing low-frequency kinetic effects, such as the Landau damping. In this turbulent scenario, estimates of the local and global scaling properties of different energy channels are obtained using a proxy of the local energy transfer. This approach provides information on the structure of energy fluxes, under the assumption that the turbulent cascade transfers most of the energy that is then dissipated at small scales by various kinetic processes in these kinds of plasmas.

1. Introduction

Space plasmas are a unique laboratory to study the transfer of energy in highly turbulent media (Bruno & Carbone 2016). In particular, the solar wind near the Earth has been continuously probed by space missions (Tu & Marsch 1995). The *in situ* measurements of this quasi-collisionless, highly variable and structured plasma show a medium in a state of fully developed turbulence. Under these conditions, turbulence is primarily

† Email address for correspondence: christian.vasconez@epn.edu.ec

originated at the Sun, and transported at high speed away from the source (Goldstein *et al.* 1996). This turbulence is then dissipated through magnetohydrodynamic (MHD) to kinetic scales, where processes such as plasma wave excitation (Valentini, Perrone & Veltri 2011), temperature anisotropy (Servidio *et al.* 2012; Perrone *et al.* 2014*a*), plasma heating (Smith *et al.* 2001; Perrone *et al.* 2014*b*; Wan *et al.* 2015; Vaivads *et al.* 2016; Valentini *et al.* 2016; Hughes *et al.* 2017; Arzamasskiy *et al.* 2019), particle energization (Gibelli, Shizgal & Yau 2010), entropy cascade (Cerri, Kunz & Califano 2018; Pezzi *et al.* 2018; Kawazura, Barnes & Schekochihin 2019) and enstrophy cascade (Servidio *et al.* 2017) are activated. Consequently, this energy cascade produces finer structures in the particle velocity distribution function (Marsch, Ao & Tu 2004; Valentini *et al.* 2008; Vásconez *et al.* 2014), and favours the presence of quasi-perpendicular wave vectors. In this environment, from a wave perspective, it is expected that kinetic Alfvén waves will be naturally developed at scales near the ion skin depth. In fact, recent observational analysis (Kiyani *et al.* 2012; Salem *et al.* 2012) and numerical simulations (TenBarge & Howes 2012; Vásconez *et al.* 2015; Pucci *et al.* 2016; Valentini *et al.* 2017) have suggested that kinetic Alfvén waves can play an important role in the dissipation of turbulent energy. The MHD approximation describes space plasma phenomenology at large enough scales (Servidio, Matthaeus & Dmitruk 2008). In this approach, a Kolmogorov-like behaviour is highly supported by observations of velocity and magnetic fluctuations showing power-law spectra and intermittency (Carbone *et al.* 2004; Greco *et al.* 2009). At the MHD scales, the solar wind has shown scale-dependent non-Gaussian statistics (Sorriso-Valvo *et al.* 1999), with non-Gaussian fluctuations observed as well in the large scales (Marino *et al.* 2012) as happens also in anisotropic fluids with waves (Feraco *et al.* 2018). The intermittent cross-scale energy transfer has been extensively described through the MHD version of the von Kármán–Howarth equation for incompressible hydrodynamic turbulence (Frisch 1995). Based on conservation laws of the MHD invariants, such law predicts the linear scaling of the mixed third-order moment of the MHD variables (Politano & Pouquet 1998). Broadly observed in numerical simulations (Sorriso-Valvo *et al.* 2002) and in space plasmas (MacBride, Forman & Smith 2005; Sorriso-Valvo *et al.* 2007; Marino *et al.* 2012; Hadid *et al.* 2018; Bandyopadhyay *et al.* 2020), the third-order law has been recently extended to include the effect of compressibility, anisotropy, Hall currents and other two-fluid effects (Galtier 2008; Andrés *et al.* 2016; Hellinger *et al.* 2018; Ferrand *et al.* 2019). At the bottom of the inertial (or Hall) range, the turbulent energy is dissipated in an efficient way as a result of inhomogeneous energy transfer, mostly occurring at small-scale vorticity filaments, rotational (or tangential) discontinuities and current sheets, among other structures (Zimbardo *et al.* 2010). At scales close to the proton inertial length and/or to the proton skin depth, pure MHD models are no longer valid (Matthaeus, Servidio & Dmitruk 2008). Kinetic processes, led by field–particle interactions, have to be considered. Observations at 1 AU show non-Maxwellian velocity distribution functions of ions and electrons in the zone where a low collision rate is measured (Leamon *et al.* 1998). Moreover, analysis of the intermittency at kinetic scales (Kiyani *et al.* 2012; Wu *et al.* 2013; Chen *et al.* 2014) has given insights into our understanding of the distribution of energy in the kinetic-scale cascade (Boldyrev & Perez 2012) and how it is dissipated at electron scales (TenBarge & Howes 2013). This has also been reported in numerical simulations (Leonardis *et al.* 2016; Franci *et al.* 2017; Grošelj *et al.* 2017). In fact, Vlasov–Maxwell numerical simulations have confirmed that particle energization is taking place near the most intense small-scale structures (Servidio *et al.* 2015). The processes responsible for such energization are not yet understood. However, mechanisms such as plasma instabilities (Primavera *et al.* 2019; Settino *et al.* 2020), wave–particle interactions (Sorriso-Valvo *et al.* 2019; Chen, Klein & Howes 2019), increase of collisions (Pezzi,

Valentini & Veltri 2016; Pezzi 2017; Pezzi *et al.* 2019) and turbulent energy dissipation due to the relation of spatially localized structures – such as thin current sheets – and magnetic reconnection sites (Carbone, Veltri & Mangeney 1990; Servidio *et al.* 2009, 2011; Cerri & Califano 2017; Franci *et al.* 2017; Yang *et al.* 2017; Camporeale *et al.* 2018), have been pointed out as good candidates. Then, direct numerical simulations have turned out to be quite useful for understanding the physics of plasmas under conditions of the near-Earth solar wind. The interested reader is referred to two recent works that present, and discuss, the current state of our understanding of plasma heating and kinetic-scale turbulence from simulations, i.e. Matthaeus *et al.* (2020) and Cerri, Groselj & Franci (2019).

In this work, we study the properties of the turbulent energy transfer in plasmas in the direct numerical simulation framework previously investigated in Perrone *et al.* (2018), which also followed the 'Turbulent Dissipation Challenge' (Parashar *et al.* 2015; Pezzi *et al.* 2017; González *et al.* 2019; Papini *et al.* 2019). In their work, Hall MHD (HMHD), Landau fluid (LF) and hybrid Vlasov–Maxwell (HVM) bidimensional simulations in turbulent regimes were ran under collisionless plasma conditions, considering an out-of-plane ambient magnetic field. Magnetic diffusivity was carefully introduced in the fluid models. The fields obtained from these simulations allow us to explore different scales linked to their respective range of validity.

This paper is organized as follows. In § 2, we briefly present the three numerical models, namely HMHD, LF and HVM, which describe – under the same two-dimensional configuration – a collisionless plasma, in typical conditions of the solar wind plasma, in a quasi-developed turbulent state. Our analyses of local and global energy transfers of this state are presented in §§ 3 and 4, respectively. We summarize and conclude in § 5.

2. Numerical models

The dynamical behaviour of a plasma strongly depends on its frequencies. Here, we provide a very brief description of the three models used in the present work, which can properly focus on different ranges of frequency. At the lowest frequencies, where ions and electrons are locked together, and the plasma behaves like an electrically conducting fluid, a MHD model is good enough to describe the system. In this study, we use a HMHD simulation, which retains dispersive effects that become relevant at scales comparable to the proton skin depth. However, when collisions can be neglected, pressure anisotropy can develop in the plasma. In this case, and at somewhat higher frequency than the previous regime, a two-fluid description is needed, since electrons and ions can move relatively to each other. Therefore, we use a LF model which is able to take into account both pressure anisotropy and low-frequency kinetic effects, such as Landau damping. At higher frequencies, a kinetic model is required. We consider the HVM approach which describes the evolution of the proton distribution function, while electrons are treated as a fluid. All three models include the electron inertial effects with a proton-to-electron mass ratio $m_p/m_e = 100$.

The HMHD and LF codes use a two-dimensional Fourier pseudo-spectral method to compute the spatial derivatives, while the time advance is performed with a third-order Runge–Kutta scheme. In these fluid codes, aliasing errors in the evaluation of nonlinear terms are treated by a $2/3$ truncation in the spectral space. In the HVM code, time advance is based on the time-splitting scheme (Cheng & Knorr 1976), combined with the current advance method (Matthews 1994). In the Vlasov equation, advection in space and velocity is solved through an explicit upwind scheme (Van Leer 1977). The HVM code uses fast Fourier transform operations only when computing the fields, and truncation is not needed since possible dealiasing errors are damped by the intrinsic dissipation of the numerical scheme.

The vector fields will evolve in a double periodic domain $D = [L, L]$, in the (x, y) plane. $L = 2\pi \times 25 d_p$ is the length of each direction x and y. This domain is discretized with $N_x = N_y = 1024$ grid points. Additionally, the HVM simulation is run in a three-dimensional velocity domain $-5v_{\mathrm{th},p} \leq \boldsymbol{v} \leq 5v_{\mathrm{th},p}$, discretized with 51^3 points, and where $v_{\mathrm{th},p} = \sqrt{T_p/m_p}$ is the thermal velocity of the protons. At $t = 0$, the equilibrium was set by a homogeneous plasma embedded in a uniform background magnetic field, $\boldsymbol{B}_0 = (0, 0, B_0)$, oriented in the z direction. We set the proton plasma beta as $\beta = 2v_{th,p}/v_A = 1$, where $v_A = B_0/\sqrt{4\pi n_0 m_p}$ is the Alfvén speed. The initial perturbation of this equilibrium is performed by velocity (and magnetic) field fluctuations with random phases in the interval $2 \leq m \leq 6$, for the wavenumbers $k = 2\pi m/L$. Although the amplitudes of the magnetic perturbations are $b/B_0 \approx 0.3$, neither density fluctuations nor parallel variances are imposed. In fluid models, a magnetic diffusivity term with a coefficient $\eta = 2 \times 10^{-2}$ has been added.

2.1. *Hall magnetohydrodynamics*

The set of HMHD equations, in a non-dimensional form, reads

$$\frac{\partial n}{\partial t} + \nabla \cdot (n\boldsymbol{u}) = 0, \tag{2.1}$$

$$\frac{\partial \boldsymbol{u}}{\partial t} + (\boldsymbol{u} \cdot \nabla)\boldsymbol{u} = -\frac{\beta}{2n}\nabla P + \frac{1}{n}[(\nabla \times \boldsymbol{B}) \times \boldsymbol{B}] - \eta_4 \nabla^4 \boldsymbol{u}, \tag{2.2}$$

$$\frac{\partial \boldsymbol{B}}{\partial t} = -\nabla \times \boldsymbol{E} - \eta_4 \nabla^4 \boldsymbol{B}, \tag{2.3}$$

$$(1 - d_e^2 \nabla^2)\boldsymbol{E} + \boldsymbol{u} \times \boldsymbol{B} - \frac{1}{n}[(\nabla \times \boldsymbol{B}) \times \boldsymbol{B}] - \eta(\nabla \times \boldsymbol{B}) = 0, \tag{2.4}$$

$$P = n^\gamma, \tag{2.5}$$

where n is the plasma density, $\boldsymbol{u}$ is the hydrodynamic velocity, $\boldsymbol{E}$ and $\boldsymbol{B}$ are the electric and magnetic fields, respectively, P is the isotropic total pressure, $\eta = 2 \times 10^{-2}$ is the magnetic diffusivity and $\gamma = 5/3$ is the adiabatic index. This non-dimensional set of equations is obtained normalizing n to $n_0 m_p$, $\boldsymbol{u}$ to the Alfvén speed v_A, t to the inverse proton cyclotron frequency $\Omega_{\mathrm{cp}}^{-1}$ and the length units to the proton skin depth $d_p = v_A/\Omega_{\mathrm{cp}}$. In Ohm's law, the electron inertia is retained in the form used in Valentini *et al.* (2007), with a non-dimensional electron skin depth $d_e^2 = m_e/m_i$ taken equal to $1/100$. For regularization purposes, and to reproduce the same-time behaviour for the maximum value of the integrated parallel current density $\langle j_z^2 \rangle$, bi-Laplacian hyperviscosity and hyperdiffusivity, with coefficients equal to $\nu_4 = \eta_4 = 5 \times 10^{-4}$, have been added to the right-hand side of velocity and magnetic field equations. Note that hyperviscosity and hyperdiffusivity strongly mitigate the effect of the electron inertia, and therefore the d_e^2 term is negligible in the present run.

2.2. *Landau fluid*

The LF system of dynamical equations solves for the evolution of the magnetic field, density, velocity, parallel and perpendicular pressures and heat fluxes in a way consistent with the low-frequency limit of the linear kinetic theory, up to a scale of the order of the ion gyroradius. The electric field is computed using a generalized Ohm's law, which includes the Hall term, together with electron inertia with the same simplified form and the same artificial mass ratio as in the HMHD case, and the same magnetic diffusivity. The electron

pressure gradient, which is formally present in Ohm's law and in the momentum equation, is here neglected to closely match the conditions of the Vlasov simulations, in which electrons are cold. The ion velocity equation reads

$$\frac{\partial \boldsymbol{u}}{\partial t} + (\boldsymbol{u}\cdot\boldsymbol{\nabla})\boldsymbol{u} = -\frac{\beta}{2n}\boldsymbol{\nabla}\cdot\boldsymbol{P} + \frac{1}{n}\left[(\boldsymbol{\nabla}\times\boldsymbol{B})\times\boldsymbol{B}\right], \tag{2.6}$$

while the density and the magnetic fields obey (2.1) and (2.3) of HMHD. The ion pressure tensor is conveniently written as $\boldsymbol{P} = p_\perp \boldsymbol{n} + p_\parallel \boldsymbol{\tau} + \boldsymbol{\Pi}$, with $\boldsymbol{\tau} = \hat{b}\otimes\hat{b}$, $\boldsymbol{n} = \boldsymbol{I} - \boldsymbol{\tau}$ and $\hat{b} = \boldsymbol{B}/|\boldsymbol{B}|$ is the unit vector along the local magnetic field. The parallel and perpendicular ion pressures obey

$$\begin{aligned}\partial_t p_\parallel + \boldsymbol{\nabla}\cdot(\boldsymbol{u}p_\parallel) + 2p_\parallel\,\hat{b}\cdot\boldsymbol{\nabla}\boldsymbol{u}\cdot\hat{b} + \hat{b}\cdot(\boldsymbol{\nabla}\cdot\boldsymbol{Q})\cdot\hat{b} \\ + \left((\boldsymbol{\Pi}\cdot\boldsymbol{\nabla}\boldsymbol{u})^S : \boldsymbol{\tau} - \boldsymbol{\Pi} : \frac{\mathrm{d}\boldsymbol{\tau}}{\mathrm{d}t}\right) = 0,\end{aligned} \tag{2.7}$$

$$\begin{aligned}\partial_t p_\perp + \boldsymbol{\nabla}\cdot(\boldsymbol{u}p_\perp) + p_\perp\boldsymbol{\nabla}\cdot\boldsymbol{u} - p_\perp\,\hat{b}\cdot\boldsymbol{\nabla}\boldsymbol{u}\cdot\hat{b} \\ + \frac{1}{2}\left(\mathrm{tr}\,\boldsymbol{\nabla}\cdot\boldsymbol{Q} - \hat{b}\cdot(\boldsymbol{\nabla}\cdot\boldsymbol{Q})\cdot\hat{b}\right) \\ + \frac{1}{2}\left(\mathrm{tr}\,(\boldsymbol{\Pi}\cdot\boldsymbol{\nabla}\boldsymbol{u})^S - (\boldsymbol{\Pi}\cdot\boldsymbol{\nabla}\boldsymbol{u})^S : \boldsymbol{\tau} + \boldsymbol{\Pi} : \frac{\mathrm{d}\boldsymbol{\tau}}{\mathrm{d}t}\right) = 0,\end{aligned} \tag{2.8}$$

thus involving the ion heat flux tensor $\boldsymbol{Q}$ along with the non-gyrotropic ion pressure tensor $\boldsymbol{\Pi}$. Here, and in (2.6), the latter will be neglected in the energy transfer budget since we are discarding finite Larmor radius effects, even though they may be relevant for energy transfers at the scale of the present simulations, and the trace term explicitly contributes to the energy conservation (see e.g. Yang *et al.* (2017) for full kinetic simulations and Cerri & Camporeale (2020) for explicit formulation in hybrid kinetic models). The non-gyrotropic pressure closure used in the present LF model (Passot *et al.* 2014) is indeed valid only in a weakly nonlinear regime, while as we numerically checked it may lead to non-physical behaviour in the present context of a too strong nonlinearity, especially when electrons are cold. So here we focused on kinetic damping only. This point should also be kept in mind when interpreting the possible discrepancies between ion-scale features obtained from HVM simulation and from the fluid simulations (see e.g. § 5).

On the same footing, the ion heat flux tensor $\boldsymbol{Q}$ is taken in its gyrotropic form, which in (2.7) and (2.8) implies $\hat{b}\cdot(\boldsymbol{\nabla}\cdot\boldsymbol{Q})\cdot\hat{b} = \boldsymbol{\nabla}\cdot(q_\parallel\hat{b}) - 2q_{\perp r}\boldsymbol{\nabla}\cdot\hat{b}$ and $(\mathrm{tr}(\boldsymbol{\nabla}\cdot\boldsymbol{Q}) - \hat{b}\cdot(\boldsymbol{\nabla}\cdot\boldsymbol{Q})\cdot\hat{b})/2 = \boldsymbol{\nabla}\cdot(q_\perp\hat{b}) + q_\perp\boldsymbol{\nabla}\cdot\hat{b}$, where the gyrotropic heat flux components obey (still neglecting higher-order non-gyrotropic contributions)

$$\begin{aligned}\partial_t q_\parallel + \boldsymbol{\nabla}\cdot(q_\parallel\boldsymbol{u}) + 3q_\parallel\hat{b}\cdot\boldsymbol{\nabla}\boldsymbol{u}\cdot\hat{b} + 3p_\parallel\left(\hat{b}\cdot\boldsymbol{\nabla}\right)\left(\frac{p_\parallel}{\rho}\right) \\ + \boldsymbol{\nabla}\cdot(\tilde{r}_{\parallel\parallel}\hat{b}) - 3\tilde{r}_{\parallel\perp}\boldsymbol{\nabla}\cdot\hat{b} = 0,\end{aligned} \tag{2.9}$$

$$\begin{aligned}\partial_t q_\perp + \boldsymbol{\nabla}\cdot(\boldsymbol{u}q_\perp) + q_\perp\boldsymbol{\nabla}\cdot\boldsymbol{u} + p_\parallel\left(\hat{b}\cdot\boldsymbol{\nabla}\right)\left(\frac{p_\perp}{\rho}\right) + \boldsymbol{\nabla}\cdot\left(\tilde{r}_{\parallel\perp}\hat{b}\right) \\ + \left(\left(p_\parallel - p_\perp\right)\frac{p_\perp}{\rho} - \tilde{r}_{\perp\perp} + \tilde{r}_{\parallel\perp}\right)\left(\boldsymbol{\nabla}\cdot\hat{b}\right) = 0.\end{aligned} \tag{2.10}$$

The gyrotropic fourth-rank cumulants $\tilde{r}_{\parallel\parallel r}$, $\tilde{r}_{\parallel\perp r}$ and $\tilde{r}_{\perp\perp r}$ needed to close the hierarchy are given by (5.1), (5.2) and (5.4) of Sulem & Passot (2015), where ion Landau damping is retained only in a quasilinear form, in the approximation discussed in Passot *et al.* (2014).

Together with the same hyperviscosity and hyperdiffusivity included in HMHD equations, additional bi-Laplacian dissipative terms have been supplemented in the equations for the density and the pressures (with coefficient equal to 2.5×10^{-3}) and in the equations for the ion heat flux (with coefficient 10^{-4}) in order to deal with the high level of compressibility in the simulation (the Mach number reaching values up to 0.4). In fact, we note that compressibility of these fluid models will be important when comparing our results.

2.3. *Hybrid Vlasov–Maxwell*

The HVM code (Valentini *et al.* 2007) solves the Vlasov equation for the proton distribution function $f = f(\boldsymbol{r}, \boldsymbol{v}, t)$, while the electron response is taken into account through a generalized Ohm's law for the electric field. The Vlasov equation, in normalized units,

$$\frac{\partial f}{\partial t} + \boldsymbol{v} \cdot \frac{\partial f}{\partial \boldsymbol{r}} + (\boldsymbol{E} + \boldsymbol{u} \times \boldsymbol{B}) \cdot \frac{\partial f}{\partial \boldsymbol{v}} = 0, \tag{2.11}$$

is solved in a 2D-3V phase-space domain (two dimensions in physical space and three dimensions in velocity space), coupling it with (2.3) and (2.4). Velocities $\boldsymbol{v}$ and $\boldsymbol{u}$ (proton bulk velocity) are scaled to v_A. Quasi-neutrality ($n = n_e = n_p$), and cold electrons, is considered. The time step is chosen in order to satisfy the Courant–Friedrichs–Lewy condition for the numerical stability. The proton distribution function is initialized with a homogeneous-density Maxwellian function. In this procedure, displacement current is neglected in the Ampère law, making the assumption of low frequencies.

3. Local energy transfer analysis

The analysis developed in this work is performed in a period of maximal turbulence activity. As described by Perrone *et al.* (2018), this state is reached at $t^* = 60\Omega_{\mathrm{cp}}^{-1}$, for the same set of simulations considered here. They established t^* after following $\langle j_z^2 \rangle$ in time, for HMHD, LF and HVM descriptions, where the same β was held in order to ensure a similar level of density fluctuations. In figure 1, we plot the out-of-plane component of the current density, $j_z(x, y)$, at $t = t^*$. The structure locations (and intensities) present on this component are consistent for the three simulations: HMHD (figure 1*a*), LF (figure 1*b*) and HVM (figure 1*c*).

Figure 2 shows the spectra of $\boldsymbol{B}$ and $\boldsymbol{u}$ for the HMHD (figure 2*a*,*d*,*g*,*j*), LF (figure 2*b*,*e*,*h*,*k*) and HVM (figure 2*c*,*f*,*i*,*l*) simulations. Magnetic field spectra (bidimensional $|B(k_x, k_y)|^2$, and reduced integrated $|B_{ki}|^2$) are presented in figure 2(*a–f*), while the velocity field spectra (bidimensional $|u(k_x, k_y)|^2$, and reduced integrated $|u_{ki}|^2$) can be seen in figure 2(*g–l*). The integrated spectra are plotted with respect to $k_i = k_x$ with a red-dashed line, and with respect to $k_i = k_y$ with a black-solid line. Bidimensional spectra maps of HMHD and LF simulations show the 2/3 truncation, which was not performed in the HVM simulation.

Considering that, in the small-scale limit, HMHD physics was observed to match hybrid kinetic model results (Vásconez *et al.* 2015; Pucci *et al.* 2016), Hellinger *et al.* (2018) presented a generalization of the von Kármán–Howarth equation for incompressible hydrodynamic turbulence, in the framework of incompressible HMHD equations. This generalization was revisited by Ferrand *et al.* (2019), who also considered homogeneous turbulence, and worked with two-point correlation tensors depending only on the relative

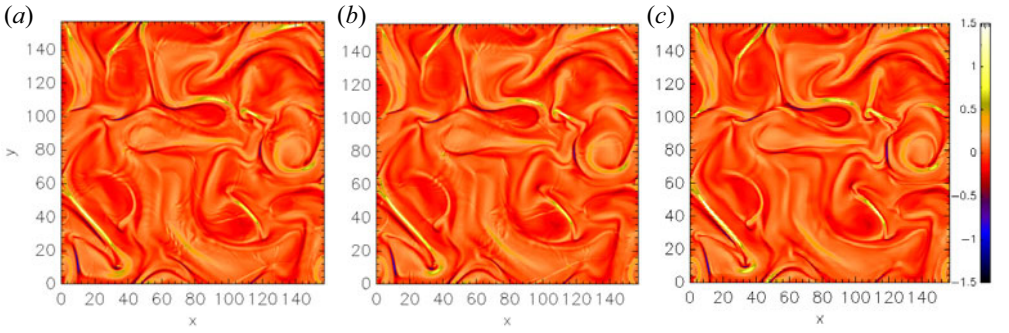

FIGURE 1. Contour plot of the out-of-plane current density $j_z(x, y)$ for HMHD (a), LF (b) and HVM (c) simulations at $t = t^*$ (see text).

displacement $\boldsymbol{\ell}$, and not on the absolute positions, as $\delta \boldsymbol{g} = \boldsymbol{g}(\boldsymbol{r} + \boldsymbol{\ell}) - \boldsymbol{g}(\boldsymbol{r})$. In this context, the mean rate of total energy injection ϵ is expressed as the combination of the third-order structure functions corresponding to the MHD turbulent cascade flux (Carbone, Sorriso-Valvo & Marino 2009; Verdini *et al.* 2015) and to Hall corrections (Galtier 2008):

$$-4\epsilon = \boldsymbol{\nabla} \cdot \langle (\delta \boldsymbol{u} \cdot \delta \boldsymbol{u}) \delta \boldsymbol{u} + (\delta \boldsymbol{B} \cdot \delta \boldsymbol{B}) \delta \boldsymbol{u} - 2(\delta \boldsymbol{u} \cdot \delta \boldsymbol{B}) \delta \boldsymbol{B} - \frac{d_p}{2} (\delta \boldsymbol{B} \cdot \delta \boldsymbol{B}) \delta \boldsymbol{j} + d_p (\delta \boldsymbol{B} \cdot \delta \boldsymbol{j}) \delta \boldsymbol{B} \rangle. \tag{3.1}$$

In fact, we can identify the single contribution of each component that corresponds to the Yaglom effect contributions,

$$\boldsymbol{Y}_1(x, y) = (\delta \boldsymbol{u} \cdot \delta \boldsymbol{u}) \delta \boldsymbol{u}, \tag{3.2}$$

$$\boldsymbol{Y}_2(x, y) = (\delta \boldsymbol{B} \cdot \delta \boldsymbol{B}) \delta \boldsymbol{u}, \tag{3.3}$$

$$\boldsymbol{Y}_3(x, y) = -2(\delta \boldsymbol{u} \cdot \delta \boldsymbol{B}) \delta \boldsymbol{B}, \tag{3.4}$$

and to the Hall effect contributions,

$$\boldsymbol{H}_1(x, y) = d_p (\delta \boldsymbol{B} \cdot \delta \boldsymbol{j}) \delta \boldsymbol{B}, \tag{3.5}$$

$$\boldsymbol{H}_2(x, y) = -\frac{d_p}{2} (\delta \boldsymbol{B} \cdot \delta \boldsymbol{B}) \delta \boldsymbol{j}. \tag{3.6}$$

In this way, (3.1) would be written as $-4\epsilon = \boldsymbol{\nabla} \cdot \langle \boldsymbol{Y}_1 + \boldsymbol{Y}_2 + \boldsymbol{Y}_3 + \boldsymbol{H}_1 + \boldsymbol{H}_2 \rangle$. Compressive fluctuations (i.e. δB and/or δn) naturally develop as the cascade proceeds towards smaller scales, becoming important at ion scales and below, even when these types of fluctuations are not directly injected at large (MHD) scales (which is the case for the simulations presented here). This effect was explicitly shown for two-dimensional simulations, for instance, in Cerri *et al.* (2017). Direct numerical simulations of compressible MHD turbulence (Andrés *et al.* 2018) and measurements in a collisionless space plasma using Magnetospheric Multiscale data in comparison with simulations of compressible HMHD turbulence (Andrés *et al.* 2019) indicate that neglecting the contribution of compressibility to the exact laws results in an underestimation of the total energy flux and dissipation rate, especially near the ion scale. However, in Andrés *et al.* (2018) it was also found that except in cases in which the largest scales already

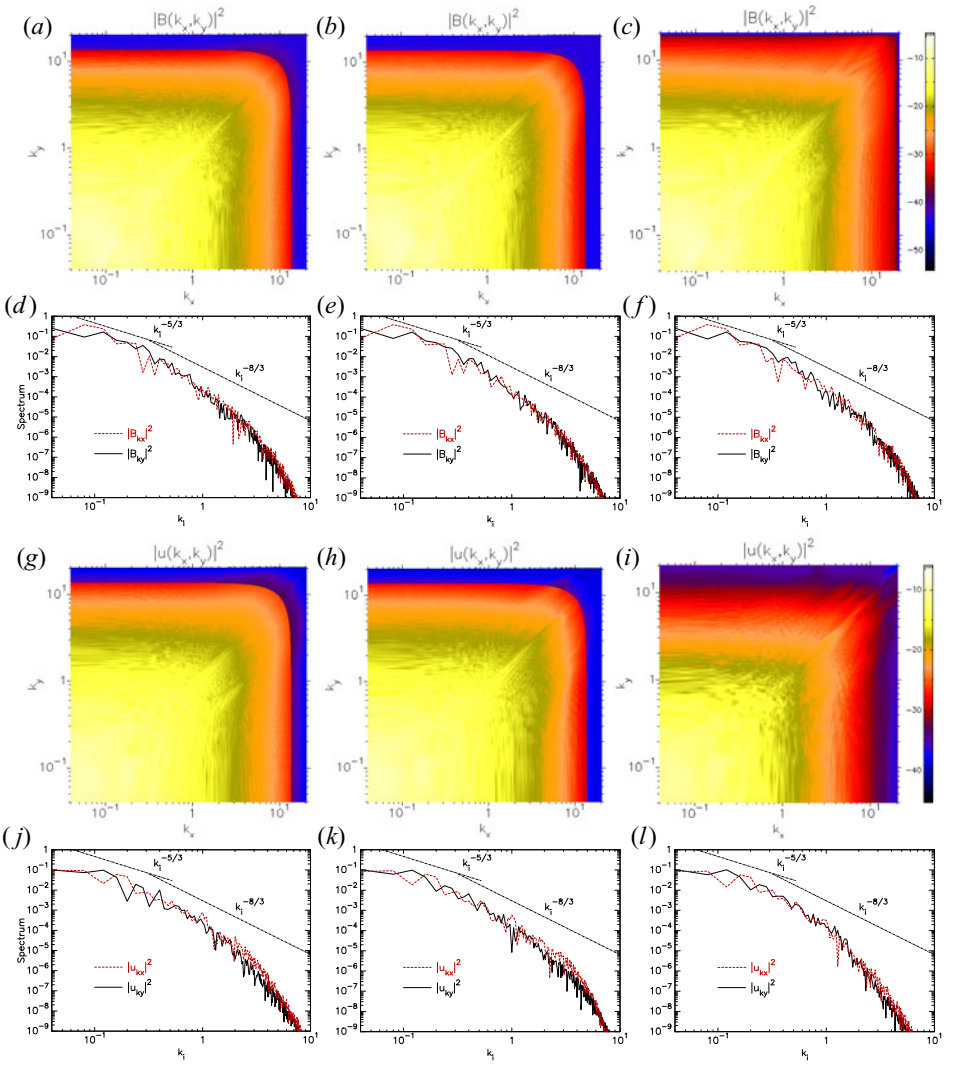

FIGURE 2. Magnetic field (*a–f*) and velocity field (*g–l*) spectra. The integrated spectra are presented with respect to k_i, $i = x$ (red-dashed line), y (black-solid line). Standard phenomenological power laws ($k_i^{-5/3}$ in the MHD range (see e.g. Frisch 1995) and $k_i^{-8/3}$ in the HMHD range (Meyrand & Galtier 2013)) are reported as reference.

display strong density fluctuations, the compressible Yaglom-like flux gives the dominant contribution to the energy flux at the MHD scales, and remains close to the incompressible Yaglom (or Politano–Pouquet) flux, while all other contributions of the compressibility to the energy flux remain small.

On the other hand, a heuristic proxy has been recently introduced. It focuses on the local turbulent energy transfer rate towards the smallest resolved scale. This proxy, named as LET, was constructed in order to extend the Yaglom law to MHD turbulence, and matches the latter law when small density fluctuations (at the scale ℓ) can be neglected (Carbone *et al.* 2009). It is estimated, for two-dimensional incompressible turbulence, through the combined third-order fluctuations of velocity, magnetic field and current

density (Sorriso-Valvo *et al.* 2018), and neglecting unity-order multiplicative factors, as

$$-2\ell\epsilon_\ell \equiv (\delta\boldsymbol{u}\cdot\delta\boldsymbol{u})\delta u_\ell + (\delta\boldsymbol{B}\cdot\delta\boldsymbol{B})\delta u_\ell - 2(\delta\boldsymbol{u}\cdot\delta\boldsymbol{B})\delta B_\ell - \frac{d_p}{2}(\delta\boldsymbol{B}\cdot\delta\boldsymbol{B})\delta j_\ell + d_p(\delta\boldsymbol{B}\cdot\delta\boldsymbol{j})\delta B_\ell. \tag{3.7}$$

Consistently with our notation, the latter equation could be rewritten as

$$-2\ell\epsilon_\ell = \epsilon_Y + \epsilon_H, \tag{3.8}$$

where $\epsilon_Y = \epsilon_{Y_1} + \epsilon_{Y_2} + \epsilon_{Y_3}$ and $\epsilon_H = \epsilon_{H_1} + \epsilon_{H_2}$. For this, $\epsilon_{Y_1} = (\delta\boldsymbol{u}\cdot\delta\boldsymbol{u})\delta u_\ell$ measures the kinetic energy available to be transported by the longitudinal component of $\delta\boldsymbol{u}$, $\epsilon_{Y_2} = (\delta\boldsymbol{B}\cdot\delta\boldsymbol{B})\delta u_\ell$ quantifies the magnetic energy that will be transported by δu_ℓ, $\epsilon_{Y_3} = -2(\delta\boldsymbol{u}\cdot\delta\boldsymbol{B})\delta B_\ell$ is related to the velocity–magnetic field correlations coupled to the longitudinal magnetic field fluctuations, $\epsilon_{H_1} = -d_p(\delta\boldsymbol{B}\cdot\delta\boldsymbol{B})\delta j_\ell/2$ indicates the quantity of magnetic energy advected by longitudinal current density field fluctuations and $\epsilon_{H_2} = d_p(\delta\boldsymbol{B}\cdot\delta\boldsymbol{j})\delta B_\ell$ is related to the magnetic–current density field correlations coupled to the longitudinal magnetic field fluctuations. In (3.7), the two latter terms vanish when $d_p \to 0$, which recovers the classic Yaglom law. It should be noted that the unaveraged third-order quantity described in (3.7) cannot be rigorously derived, and may therefore display convergence issues. In other words, it does not describe a turbulent cascade, but just the local contribution of the turbulent fluctuations to the energy transfer. On the other hand, its use as a proxy is partly supported by the existence of local versions of the third-order scaling law, whose rigorous derivation is based on the use of scale- and space-localized filters (Duchon & Robert 2000; Eyink 2003; Camporeale *et al.* 2018; Coburn & Sorriso-Valvo 2019).

Since we want to explore the energy flux distribution resulting from the turbulent nonlinear transfer, we first focus on the scale $\sim d_p$, i.e. at the bottom of the inertial range, where the intermittent structures carrying most of the energy have been formed. As we noted in § 2, $N_x = N_y = 1024$, then $\Delta x = \Delta y \approx 0.15$, resulting in $\ell \approx d_p$. At this scale, we will identify the Yaglom $\boldsymbol{Y}_m(x, y) = (\boldsymbol{Y}_{mx} + \boldsymbol{Y}_{my})/2$ and Hall $\boldsymbol{H}_n(x, y) = (\boldsymbol{H}_{nx} + \boldsymbol{H}_{ny})/2$ contributions, according to their spatial distribution, where $m = 1, 2, 3$ and $n = 1, 2$. These two-dimensional maps are presented in figure 3 (HMHD), figure 4 (LF) and figure 5 (HVM). They clearly highlight the intermittent nature of the cross-scale energy transfer. This is evidenced by the presence of strong contributions to the scaling law in small-scale localized, sparse structures. Most of the energy transfer, and consequently of the energy dissipation, is taking place at those locations, which was also reported in Yang *et al.* (2017) and in Camporeale *et al.* (2018). This feature may be consistent with the idea that reconnection of current sheets, and the formation of coherent structures, could provide a viable mechanism for (likely cross-scale) energy transfer across ion-kinetic scales (Cerri & Califano 2017; Franci *et al.* 2017). It is interesting to note that different terms of the HMHD law may present similar structures at the same locations. However, in several instances the structures of different contributions are not collocated, suggesting that the nature of the fluctuations producing the energy transfer may change with position, possibly enabling different dissipation mechanisms (Sorriso-Valvo *et al.* 2019). It is also apparent that most of the more intense structures are positive, suggesting that the energy is being transferred towards the small scales in a 'direct' cascade. However, several negative structures are also present, where the contribution from the various terms is acting so as to remove energy from the smaller scales. We do not imply here that the sign of the local contributions is related to the cascade direction, and the latest statements should be

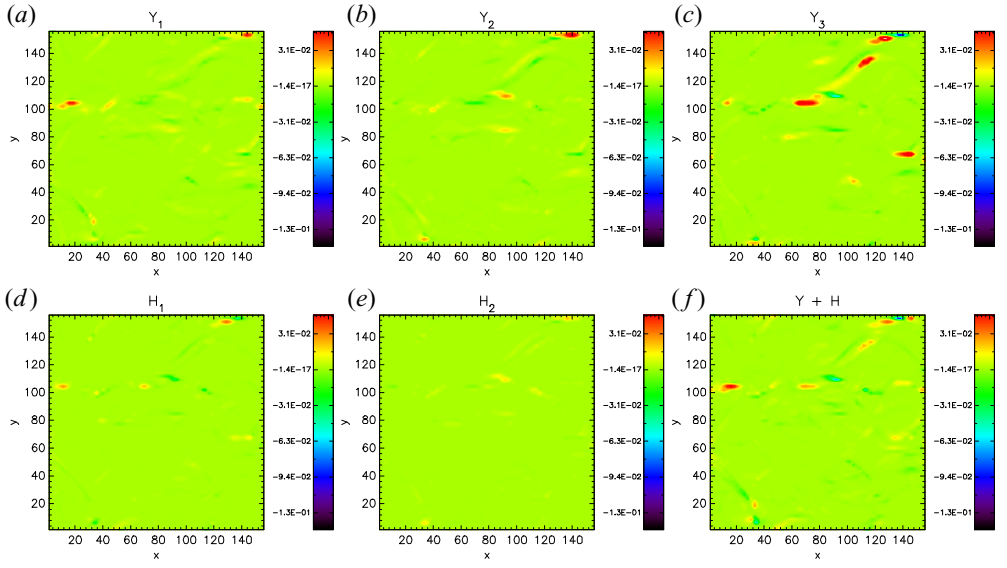

FIGURE 3. The HMHD simulation. Bidimensional maps of Yaglom components $\boldsymbol{Y}_1$ (equation (3.2)), $\boldsymbol{Y}_2$ (equation (3.3)) and $\boldsymbol{Y}_3$ (equation (3.4)); and Hall components $\boldsymbol{H}_1$ (equation (3.5)) and $\boldsymbol{H}_2$ (equation (3.6)), of the mean rate of total energy injection, estimated at the scale $\ell \simeq d_p$.

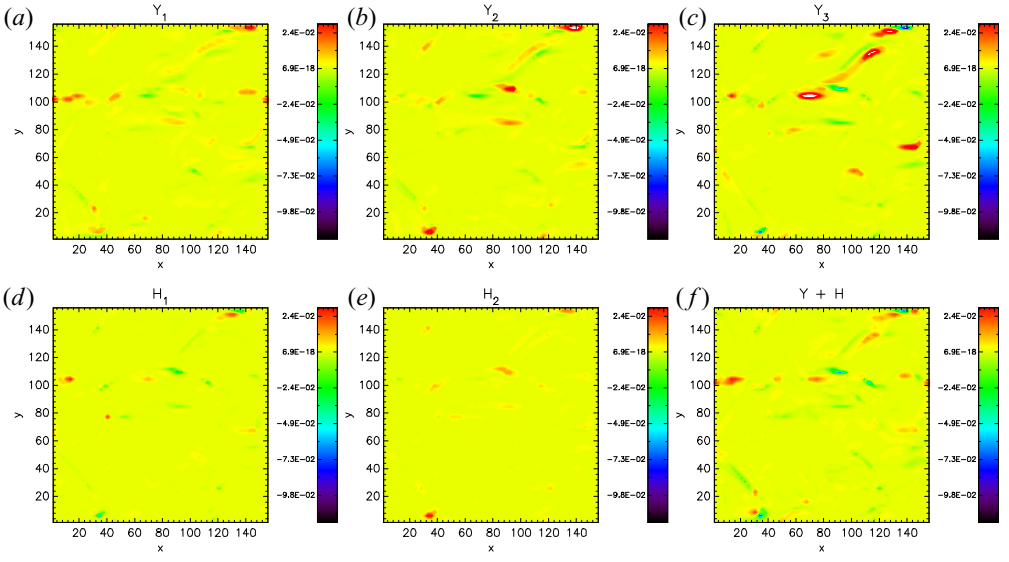

FIGURE 4. The LF simulation. Bidimensional maps of Yaglom components $\boldsymbol{Y}_1$ (equation (3.2)), $\boldsymbol{Y}_2$ (equation (3.3)) and $\boldsymbol{Y}_3$ (equation (3.4)); and Hall components $\boldsymbol{H}_1$ (equation (3.5)) and $\boldsymbol{H}_2$ (equation (3.6)), of the mean rate of total energy injection, estimated at the scale $\ell \simeq d_p$.

taken as a qualitative indication. Note that the overall energy flux will result from the average over the whole domain, and is mostly positive, as expected and as we discuss in the next section. Comparing the different simulations reveals that the various terms have similar behaviour. In particular, the $\boldsymbol{Y}_3$ term seems to be dominating in the simulations.

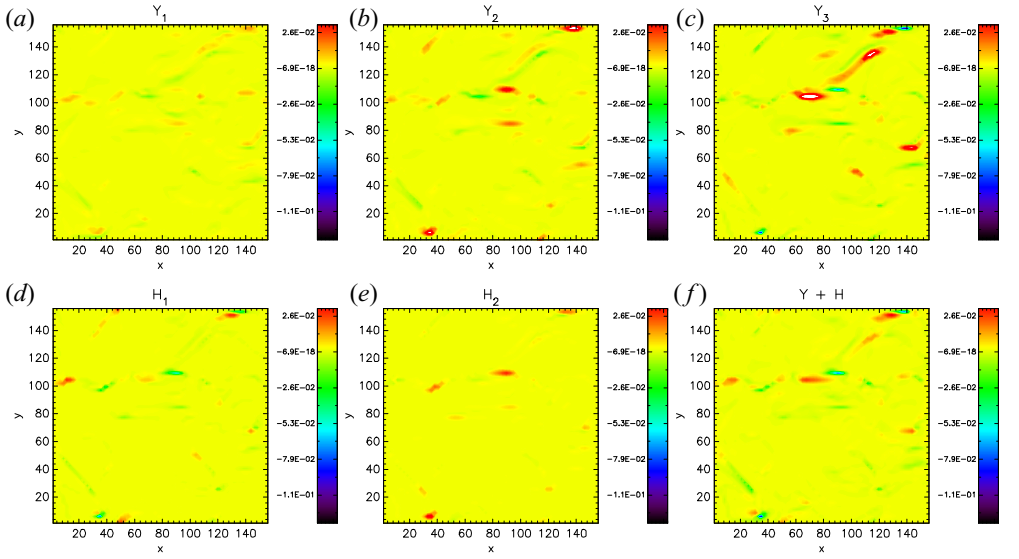

FIGURE 5. The HVM simulation. Two-dimensional maps of Yaglom components $\boldsymbol{Y}_1$ (equation (3.2)), $\boldsymbol{Y}_2$ (equation (3.3)) and $\boldsymbol{Y}_3$ (equation (3.4)); and Hall components $\boldsymbol{H}_1$ (equation (3.5)) and $\boldsymbol{H}_2$ (equation (3.6)), of the mean rate of total energy injection, estimated at the scale $\ell \simeq d_p$.

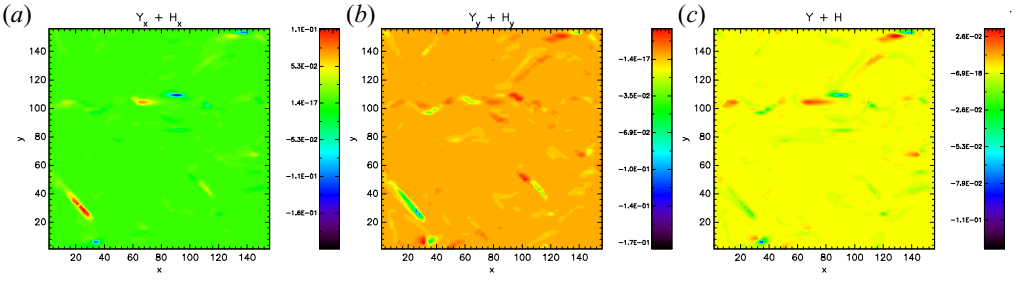

FIGURE 6. The x (a) and y (b) components of the term $\boldsymbol{Y} + \boldsymbol{H}$ (c), computed from the HVM simulation, estimated at the scale $\ell \simeq d_p$.

Interestingly, in the HMHD simulation the Hall terms appear weaker than in the two other simulations. This observation will be discussed later.

Finally, the maps of $\boldsymbol{Y} + \boldsymbol{H}$ are separated by components in figure 6 for the HVM simulation (similar behaviour was found in HMHD and LF simulations – not shown here). While the general behaviour is similar, some differences between the two components of the energy transfer exist, possibly an effect of the finite size of the ensemble.

4. Global energy transfer analysis

We continue our analysis computing the local turbulent energy transfer rate $-2\epsilon_\ell$ across the scales ℓ. Figure 7 presents the averaged (3.7) over the whole domain, corresponding to the HMHD (figure 7*a*), LF (figure 7*b*) and HVM (figure 7*c*) simulations. We separate the Yaglom (black-solid line) and Hall (red-solid line) contributions in order to highlight their relative amplitude across the scales ℓ. The sum of both contributions, giving the Hall–Yaglom law, is plotted with asterisks. As already observed in the previous section, in the HMHD and LF simulations, the Hall contribution $\epsilon_{H(\ell)}$ is always less than the

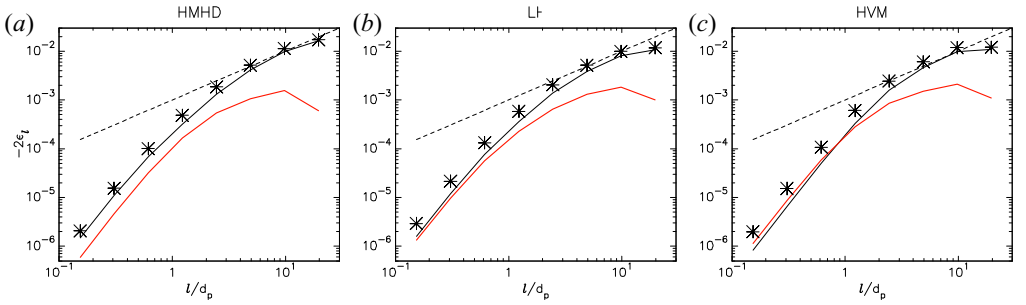

FIGURE 7. Cascade rate $-2\epsilon_\ell$ law as a function of the scale ℓ, conducted in the HMHD (a), LF (b) and HVM (c) simulations. The contributing terms ϵ_Y (black-solid line) and ϵ_H (red-solid line) are presented together with their direct sum (asterisks). The dashed line represents the linear scaling.

Yaglom one. However, both contributions become closer for scales $\ell \lesssim d_p$. In the case of the HVM simulation, that occurs in the range $\ell \lesssim d_p$, $\epsilon_{H(\ell)} > \epsilon_{Y(\ell)}$. Then, at $\ell \approx d_p$, $\epsilon_{Y(\ell)}$ becomes more relevant and remains so for larger scales. This behaviour is consistent with the settings of our simulations, where the mean field is out-of-plane, and there is strong whistler/magnetosonic activity. Linear theory studied by Camporeale & Burgess (2017) supports this interpretation, which is also compatible with earlier results from hybrid and full kinetic two-dimensional simulations reported by Cerri *et al.* (2016) and by Grošelj *et al.* (2017). If we recall that the Hall term ϵ_H manifests itself through compressible activity, the cascade rates are expected to be affected in the fluid simulations; while in the HVM simulation, this compressible activity is suppressed through in-plane Landau damping and ion-cyclotron resonances, which re-inject in the system incompressible Alfvénic-like fluctuations. In this two-dimensional setting, the LF model, in which Landau dissipation is introduced at a quasilinear level, partially quenches compressible fluctuations, but not as efficiently as the HVM one. In addition, we can confirm that in the interval $2d_p \lesssim \ell \lesssim 10d_p$ (roughly corresponding to the MHD turbulence range), the scaling of $-2\epsilon_\ell$ is compatible with a linear scaling law (black-dashed line) for our three cases of study, as previously reported by Sorriso-Valvo *et al.* (2018).

Moreover, in figure 8 we can see how Yaglom $-\epsilon_{Y_m}$ and Hall $-\epsilon_{H_n}$ terms are supporting the latter global behaviour. We use open diamonds to picture the positive terms, while negative quantities are plotted with red-filled diamonds. Figure 8(a,d,g,j,m) shows the HMHD simulation results, figure 8(b,e,h,k,n) corresponds to the LF simulation, while the results from the HVM simulation are presented in figure 8(c,f,i,l,o). If we focus on the amplitude and sign of these quantities, we cannot note substantial differences between the individual Hall contributions among the simulations. However, the sign of $-\epsilon_{Y_2}$ (associated with the magnetic energy transported by the velocity field) is passing from negative to positive at $\sim 2d_p$ in the HVM simulation. This is not seen in the HMHD and LF counterparts.

Finally, we use our results to compare the amplitude of each of the Yaglom and Hall terms across the scales. In figure 9, we present these comparisons for the Yaglom terms: $\epsilon_{Y_1}/\epsilon_{Y_3}$ (figure 9a) and $\epsilon_{Y_2}/\epsilon_{Y_3}$ (figure 9b). Comparison of Hall terms $\epsilon_{H_1}/\epsilon_{H_2}$ is shown in figure 9(c). Figure 9(d) shows ϵ_Y/ϵ_H. Black-solid line represents the HMHD simulation, blue-dash-dotted line represents the LF results and red-dashed line is for the HVM simulation. From a global point of view, we note that the comparisons computed from the LF and HVM simulations are quite similar, especially for scales $\ell \lesssim 10d_p$. After this

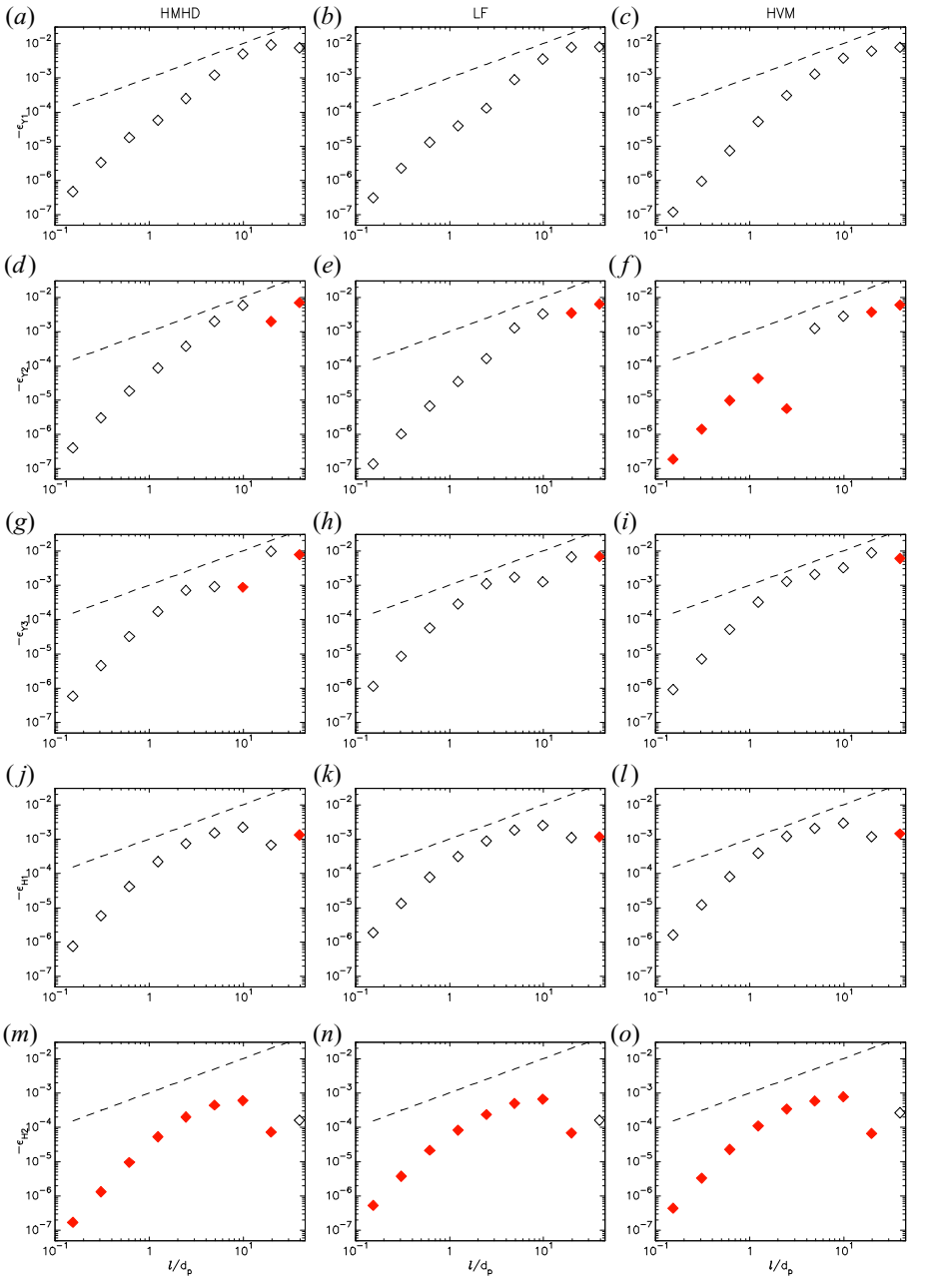

FIGURE 8. Terms $-\epsilon_{Y_1}$ (*a–c*), $-\epsilon_{Y_2}$ (*d–f*), $-\epsilon_{Y_3}$ (*g–i*), $-\epsilon_{H_1}$ (*j–l*) and $-\epsilon_{H_2}$ (*m–o*). The components are computed from the HMHD (*a*,*d*,*g*,*j*,*m*), LF (*b*,*e*,*h*,*k*,*n*) and HVM (*c*,*f*,*i*,*l*,*o*) simulations. Open diamonds correspond to the positive sign, while red-filled diamonds show negative values. Linear scaling is plotted with a black-dashed line.

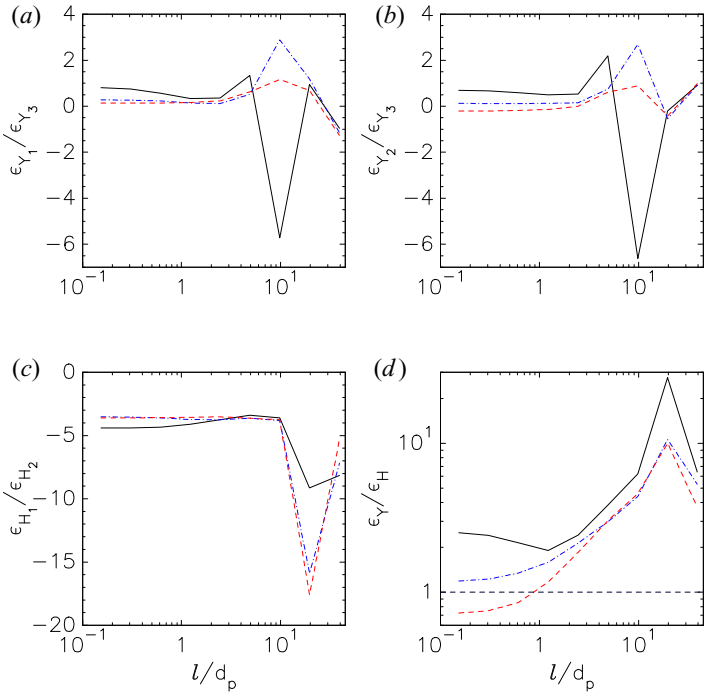

FIGURE 9. (*a*,*b*) Comparison of the Yaglom terms ϵ_{Y_1} and ϵ_{Y_2}, with respect to ϵ_{Y_3}. (*c*) Comparison between the Hall terms (ϵ_{H_1} and ϵ_{H_2}). (*d*) Comparison between ϵ_Y and ϵ_H, where the horizontal grey-dashed line marks the barrier of $\epsilon_Y/\epsilon_H = 1$. Black-solid line corresponds to the HMHD simulation, blue-dash-dotted line corresponds to the LF simulation and the HVM simulation is represented by the red-dashed line.

range, the sign of ϵ_{Y_3} fluctuates with respect to that of ϵ_{Y_1} and ϵ_{Y_2}. On the other hand, the sign of ϵ_{H_1}, as compared with ϵ_{H_2}, remains negative for all of the scales. Once again, the LF and HVM simulations seem quite similar when comparing the Hall terms. The comparison ϵ_Y/ϵ_H shows that the HVM simulation is useful for study the transition from fluid to kinetic scales ($\sim d_p$) as we can see when comparing this ratio.

5. Discussion and conclusions

In this paper we study the properties of energy transfer contributions in collisionless turbulent plasmas. For this scope, the heuristic proxy LET was computed for three numerical simulations (HMHD, LF and HVM) of a quasi-steady state of turbulence. Moreover, this study would also be aligned to the 'Turbulent Dissipation Challenge' (Parashar *et al.* 2015), as we test the LET proxy on three different numerical models (which use different numerical schemes) under the same initial conditions, with similar physical and numerical parameters. We have in mind that each of these models have their own characteristic scale. In the HVM model, this scale corresponds to the proton skin depth. In the fluid models, this scale corresponds to the dissipative scale, where the energy is dissipated by viscous and resistive effects.

In figures 3–5, we presented bidimensional maps for each of the simulations, and for the scale $\ell \approx d_p$. In particular, in figure 6 we show the location and intensity of the structures where most of the energy is contributing to the cross-scale transfer.

Then, figure 7 tests the $-2\epsilon_\ell$ cascade-rate definition ((3.7)). Here, when only the global contribution of $\epsilon_Y + \epsilon_H$ is plotted (asterisks), no strong differences are seen between our set of simulations. However, when ϵ_Y (black-solid line) and ϵ_H (red-solid line) are separated, we note that in the HVM simulation $\epsilon_H > \epsilon_Y$ for scales $\ell \lesssim d_p$, not observed for the other simulations. This difference is likely due to the slightly larger values and fluctuations of the current observed in the HVM case (see, for example, figure 1 in Perrone *et al.* (2018)). We further point out that a net contribution in the energy budget might be due to the pressure anisotropy, which is not taken into account in the fluid Yaglom theory as briefly discussed in § 3.

We observe that $\epsilon_{Y_2} \sim (\delta \boldsymbol{B} \cdot \delta \boldsymbol{u})\delta u_\ell$ have opposite sign – for the majority of the scales – in the HVM simulation, with respect to the fluid simulations (figure 6). Also for this parameter, a change of monotonicity may be noticed in the interval $2d_p \lesssim \ell \lesssim 10d_p$ (roughly corresponding to the MHD turbulence range) only in the HVM simulation. The reason for this behaviour is not fully understood.

Finally, the comparisons made in figure 9 show similarity between our set of simulations for scales $\ell \lesssim 2d_p$. After this range, the contribution of ϵ_{Y_3} decreases with respect to ϵ_{Y_1} (figure 9*a*) and ϵ_{Y_2} (figure 9*b*). A similar behaviour, related to the direction of the energy cascade, is seen when comparing the Hall terms (figure 9*c*), where the amplitude of ϵ_{H_2} decreases more about one decade with respect to ϵ_{H_1} when $\ell \gtrsim 10d_p$.

Our overall conclusion is that the three simulations are similar, but not exactly identical, with respect to the local and global turbulent energy transfer. This implies that a cross-scale interconnection exists between fluid and kinetic dynamics, so that not only does the turbulent cascade drive the small-scale kinetic processes, but the latter also controls the cascade, acting as a form of dynamical dissipation. Further studies are needed to describe in more detail such interconnection. Work in progress includes the extension of energy transfer analysis in three-dimensional simulations and a multifractal study of the turbulence (Primavera & Florio 2019).

Acknowledgements

C.L.V. was partially supported by EPN projects PIM-19-01, PII-DFIS-2019-01 and PII-DFIS-2019-04. L.S.-V. was funded by the Swedish Contingency Agency, grant 2016-2102. R.M. acknowledges support from the project 'EVENTFUL' (ANR-20-CE30-0011), funded by the French Agence nationale de la recherche (ANR) through the programme ANR AAPG2020 CE30 JCJC. C.L.V. acknowledges valuable discussions with O. Pezzi and A. Enriquez.

REFERENCES

ANDRÉS, N., MININNI, P. D., DMITRUK, P. & GOMEZ, D. O. 2016 von Kármán–Howarth equation for three-dimensional two-fluid plasmas. *Phys. Rev.* E **93** (6), 063202.

ANDRÉS, N., SAHRAOUI, F., GALTIER, S., HADID, L. Z., DMITRUK, P. & MININNI, P. D. 2018 Energy cascade rate in isothermal compressible magnetohydrodynamic turbulence. *J. Plasma Phys.* **84** (4), 905840404.

ANDRÉS, N., SAHRAOUI, F., GALTIER, S., HADID, L. Z., FERRAND, R. & HUANG, S. Y. 2019 Energy cascade rate measured in a collisionless space plasma with MMS data and compressible hall magnetohydrodynamic turbulence theory. *Phys. Rev. Lett.* **123** (24), 245101.

Arzamasskiy, L., Kunz, M. W., Chandran, B. D. G. & Quataert, E. 2019 Hybrid-kinetic simulations of ion heating in Alfvénic turbulence. *Astrophys. J.* **879** (1), 53.

Bandyopadhyay, R., Goldstein, M. L., Maruca, B. A., Matthaeus, W. H., Parashar, T. N., Ruffolo, D., Chhiber, R., Usmanov, A., Chasapis, A., Qudsi, R., *et al.* 2020 Enhanced energy transfer rate in solar wind turbulence observed near the Sun from Parker Solar Probe. *Astrophys. J. Suppl. Ser.* **246**, 48.

Boldyrev, S. & Perez, J. C. 2012 Spectrum of kinetic-Alfvén turbulence. *Astrophys. J. Lett.* **758** (2), L44.

Bruno, R. & Carbone, V. 2016 *Turbulence in the Solar Wind*. Springer.

Camporeale, E. & Burgess, D. 2017 Comparison of linear modes in kinetic plasma models. *J. Plasma Phys.* **83** (2), 535830201.

Camporeale, E., Sorriso-Valvo, L., Califano, F. & Retinò, A. 2018 Coherent structures and spectral energy transfer in turbulent plasma: a space-filter approach. *Phys. Rev. Lett.* **120** (12), 125101.

Carbone, V., Bruno, R., Sorriso-Valvo, L. & Lepreti, F. 2004 Intermittency of magnetic turbulence in slow solar wind. *Planet. Space Sci.* **52** (10), 953–956.

Carbone, V., Marino, R., Sorriso-Valvo, L., Noullez, A. & Bruno, R. 2009 Scaling laws of turbulence and heating of fast solar wind: the role of density fluctuations. *Phys. Rev. Lett.* **103** (6), 061102.

Carbone, V., Sorriso-Valvo, L. & Marino, R. 2009 On the turbulent energy cascade in anisotropic magnetohydrodynamic turbulence. *Europhys. Lett.* **88** (2), 25001.

Carbone, V., Veltri, P. & Mangeney, A. 1990 Coherent structure formation and magnetic field line reconnection in magnetohydrodynamic turbulence. *Phys. Fluids* A **2** (8), 1487–1496.

Cerri, S. S. & Camporeale, E. 2020 Space-filter techniques for quasi-neutral hybrid-kinetic models. *Phys. Plasmas* **27**, 082102.

Cerri, S. S., Franci, L., Califano, F., Landi, S. & Hellinger, P. 2017 Plasma turbulence at ion scales: a comparison between particle in cell and Eulerian hybrid-kinetic approaches. *J. Plasma Phys.* **83** (2), 705830202.

Cerri, S. S., Kunz, M. W. & Califano, F. 2018 Dual phase-space cascades in 3D hybrid-Vlasov–Maxwell turbulence. *Astrophys. J. Lett.* **856** (1), L13.

Cerri, S. S. & Califano, F. 2017 Reconnection and small-scale fields in 2D-3V hybrid-kinetic driven turbulence simulations. *New J. Phys.* **19** (2), 025007.

Cerri, S. S., Califano, F., Jenko, F., Told, D. & Rincon, F. 2016 Subproton-scale cascades in solar wind turbulence: driven hybrid-kinetic simulations. *Astrophys. J. Lett.* **822** (1), L12.

Cerri, S. S., Groselj, D. & Franci, L. 2019 Kinetic plasma turbulence: recent insights and open questions from 3D3V simulations. *Front. Astron. Space Sci.* **6**, 64.

Chen, C. H. K., Klein, K. G. & Howes, G. G. 2019 Evidence for electron landau damping in space plasma turbulence. *Nat. Commun.* **10** (1), 1–8.

Chen, C. H. K., Sorriso-Valvo, L., Šafránková, J. & Němeček, Z. 2014 Intermittency of solar wind density fluctuations from ion to electron scales. *Astrophys. J. Lett.* **789** (1), L8.

Cheng, C.-Z. & Knorr, G. 1976 The integration of the Vlasov equation in configuration space. *J. Comput. Phys.* **22** (3), 330–351.

Coburn, J. T. & Sorriso-Valvo, L. 2019 Energy transfer in incompressible magnetohydrodynamics: the filtered approach. *Fluids* **4**, 163.

Duchon, J. & Robert, R. 2000 Inertial energy dissipation for weak solutions of incompressible euler and Navier–Stokes equations. *Nonlinearity* **13**, 249.

Eyink, G. L. 2003 Local 4/5-law and energy dissipation anomaly in turbulence. *Nonlinearity* **16**, 137.

Feraco, F., Marino, R., Pumir, A., Primavera, L., Mininni, P. D., Pouquet, A. & Rosenberg, D. 2018 Vertical drafts and mixing in stratified turbulence: sharp transition with Froude number. *Europhys. Lett.* **123**, 4402.

Ferrand, R., Galtier, S., Sahraoui, F., Meyrand, R., Andrés, N. & Banerjee, S. 2019 On exact laws in incompressible hall magnetohydrodynamic turbulence. *Astrophys. J.* **881** (1), 50.

FRANCI, L., CERRI, S. S., CALIFANO, F., LANDI, S., PAPINI, E., VERDINI, A., MATTEINI, L., JENKO, F. & HELLINGER, P. 2017 Magnetic reconnection as a driver for a sub-ion-scale cascade in plasma turbulence. *Astrophys. J. Lett*. **850** (1), L16.

FRISCH, U. 1995 *Turbulence: The Legacy of AN Kolmogorov*. Cambridge University Press.

GALTIER, S. 2008 von Kármán–Howarth equations for hall magnetohydrodynamic flows. *Phys. Rev.* E **77** (1), 015302.

GIBELLI, L., SHIZGAL, B. D. & YAU, A. W. 2010 Ion energization by wave–particle interactions: comparison of spectral and particle simulation solutions of the Vlasov equation. *Comput. Maths Appl*. **59** (8), 2566–2581.

GOLDSTEIN, B. E., NEUGEBAUER, M., PHILLIPS, J. L., BAME, S., GOSLING, J. T., MCCOMAS, D., WANG, Y. M., SHEELEY, N. R. & SEUSS, S. T. 1996 Ulysses plasma parameters: latitudinal, radial, and temporal variations. *Astron. Astrophys*. **316**, 296–303.

GONZÁLEZ, C. A., PARASHAR, T. N., GOMEZ, D., MATTHAEUS, W. H. & DMITRUK, P. 2019 Turbulent electromagnetic fields at sub-proton scales: two-fluid and full-kinetic plasma simulations. *Phys. Plasmas* **26** (1), 012306.

GRECO, A., MATTHAEUS, W. H., SERVIDIO, S., CHUYCHAI, P. & DMITRUK, P. 2009 Statistical analysis of discontinuities in solar wind ace data and comparison with intermittent MHD turbulence. *Astrophys. J. Lett*. **691** (2), L111.

GROŠELJ, D., CERRI, S. S., NAVARRO, A. B., WILLMOTT, C., TOLD, D., LOUREIRO, N. F., CALIFANO, F. & JENKO, F. 2017 Fully kinetic versus reduced-kinetic modeling of collisionless plasma turbulence. *Astrophys. J*. **847** (1), 28.

HADID, L. Z., SAHRAOUI, F., GALTIER, S. & HUANG, S. Y. 2018 Compressible magnetohydrodynamic turbulence in the Earth's magnetosheath: estimation of the energy cascade rate using in situ spacecraft data. *Phys. Rev. Lett*. **120**, 055102.

HELLINGER, P., VERDINI, A., LANDI, S., FRANCI, L. & MATTEINI, L. 2018 von Kármán–Howarth equation for hall magnetohydrodynamics: hybrid simulations. *Astrophys. J*. **857** (2), L19.

HUGHES, R. S., GARY, S. P., WANG, J. & PARASHAR, T. N. 2017 Kinetic Alfvén turbulence: electron and ion heating by particle-in-cell simulations. *Astrophys. J. Lett*. **847** (2), L14.

KAWAZURA, Y., BARNES, M. & SCHEKOCHIHIN, A. A. 2019 Thermal disequilibration of ions and electrons by collisionless plasma turbulence. *Proc. Natl Acad. Sci*. **116** (3), 771–776.

KIYANI, K. H., CHAPMAN, S. C., SAHRAOUI, F., HNAT, B., FAUVARQUE, O. & KHOTYAINTSEV, Y. V. 2012 Enhanced magnetic compressibility and isotropic scale invariance at sub-ion Larmor scales in solar wind turbulence. *Astrophys. J*. **763** (1), 10.

LEAMON, R. J., SMITH, C. W., NESS, N. F., MATTHAEUS, W. H. & WONG, H. K. 1998 Observational constraints on the dynamics of the interplanetary magnetic field dissipation range. *J. Geophys. Res*. **103** (A3), 4775–4787.

LEONARDIS, E., SORRISO-VALVO, L., VALENTINI, F., SERVIDIO, S., CARBONE, F. & VELTRI, P. 2016 Multifractal scaling and intermittency in hybrid Vlasov–Maxwell simulations of plasma turbulence. *Phys. Plasmas* **23** (2), 022307.

MACBRIDE, B. T., FORMAN, M. A. & SMITH, C. W. 2005 Turbulence and third moment of fluctuations: Kolmogorov's 4/5 law and its MHD analogues in the solar wind. In *Solar Wind 11/SOHO 16, Connecting Sun and Heliosphere* (ed. B. Fleck, T. H. Zurbuchen & H. Lacoste). ESA Special Publication.

MARINO, R., SORRISO-VALVO, L., D'AMICIS, R., CARBONE, V., BRUNO, R. & VELTRI, P. 2012 On the occurrence of the third-order scaling in high latitude solar wind. *Astrophys. J*. **750**, 41.

MARSCH, E., AO, X.-Z. & TU, C.-Y. 2004 On the temperature anisotropy of the core part of the proton velocity distribution function in the solar wind. *J. Geophys. Res*. **109** (A4), A04102.

MATTHAEUS, W. H., SERVIDIO, S. & DMITRUK, P. 2008 Comment on "kinetic simulations of magnetized turbulence in astrophysical plasmas". *Phys. Rev. Lett*. **101** (14), 149501.

MATTHAEUS, W. H., YANG, Y., WAN, M., PARASHAR, T. N., BANDYOPADHYAY, R., CHASAPIS, A., PEZZI, O. & VALENTINI, F. 2020 Pathways to dissipation in weakly collisional plasmas. *Astrophys. J*. **891** (1), 101.

MATTHEWS, A. P. 1994 Current advance method and cyclic leapfrog for 2D multispecies hybrid plasma simulations. *J. Comput. Phys*. **112** (1), 102–116.

MEYRAND, R. & GALTIER, S. 2013 Anomalous $k_{\perp}^{-8/3}$ spectrum in electron magnetohydrodynamic turbulence. *Phys. Rev. Lett*. **111**, 264501.

PAPINI, E., FRANCI, L., LANDI, S., VERDINI, A., MATTEINI, L. & HELLINGER, P. 2019 Can hall magnetohydrodynamics explain plasma turbulence at sub-ion scales? *Astrophys. J*. **870** (1), 52.

PARASHAR, T. N., SALEM, C., WICKS, R. T., KARIMABADI, H., GARY, S. P. & MATTHAEUS, W. H. 2015 Turbulent dissipation challenge: a community-driven effort. *J. Plasma Phys*. **81** (5), 905810513.

PASSOT, T., HENRI, P., LAVEDER, D. & SULEM, P. L. 2014 Fluid simulations of ion scale plasmas with weakly distorted magnetic fields. *Eur. Phys. J.* D **68**, 207.

PERRONE, D., BOUROUAINE, S., VALENTINI, F., MARSCH, E. & VELTRI, P. 2014*a* Generation of temperature anisotropy for alpha particle velocity distributions in solar wind at 0.3 AU: Vlasov simulations and Helios observations. *J. Geophys. Res*. **119** (4), 2400–2410.

PERRONE, D., PASSOT, T., LAVEDER, D., VALENTINI, F., SULEM, P. L., ZOUGANELIS, I., VELTRI, P. & SERVIDIO, S. 2018 Fluid simulations of plasma turbulence at ion scales: comparison with Vlasov–Maxwell simulations. *Phys. Plasmas* **25** (5), 052302.

PERRONE, D., VALENTINI, F., SERVIDIO, S., DALENA, S. & VELTRI, P. 2014*b* Analysis of intermittent heating in a multi-component turbulent plasma. *Eur. Phys. J.* D **68** (7), 209.

PEZZI, O. 2017 Solar wind collisional heating. *J. Plasma Phys*. **83** (3), 555830301.

PEZZI, O., PARASHAR, T. N., SERVIDIO, S., VALENTINI, F., VÁSCONEZ, C. L., YANG, Y., MALARA, F., MATTHAEUS, W. H. & VELTRI, P. 2017 Colliding Alfvénic wave packets in magnetohydrodynamics, hall and kinetic simulations. *J. Plasma Phys*. **83** (1), 705830108.

PEZZI, O., PERRONE, D., SERVIDIO, S., VALENTINI, F., SORRISO-VALVO, L. & VELTRI, P. 2019 Proton–proton collisions in the turbulent solar wind: hybrid Boltzmann–Maxwell simulations. *Astrophys. J*. **887** (2), 208.

PEZZI, O., SERVIDIO, S., PERRONE, D., VALENTINI, F., SORRISO-VALVO, L., GRECO, A., MATTHAEUS, W. H. & VELTRI, P. 2018 Velocity-space cascade in magnetized plasmas: numerical simulations. *Phys. Plasmas* **25** (6), 060704.

PEZZI, O., VALENTINI, F. & VELTRI, P. 2016 Collisional relaxation of fine velocity structures in plasmas. *Phys. Rev. Lett*. **116** (14), 145001.

POLITANO, H. & POUQUET, A. 1998 Dynamical length scales for turbulent magnetized flows. *Geophys. Res. Lett*. **25** (3), 273–276.

PRIMAVERA, L. & FLORIO, E. 2020 Parallel algorithms for multifractal analysis of river networks. In *Numerical Computations: Theory and Algorithms. NUMTA 2019. Lecture Notes in Computer Science* (ed. Y. Sergeyev & D. Kvasov), vol 11973. Springer, Cham.

PRIMAVERA, L., MALARA, F., SERVIDIO, S., NIGRO, G. & VELTRI, P. 2019 Parametric instability in two-dimensional Alfvénic turbulence. *Astrophys. J*. **880** (2), 156.

PUCCI, F., VÁSCONEZ, C. L., PEZZI, O., SERVIDIO, S., VALENTINI, F., MATTHAEUS, W. H. & MALARA, F. 2016 From Alfvén waves to kinetic Alfvén waves in an inhomogeneous equilibrium structure. *J. Geophys. Res*. **121** (2), 1024–1045.

SALEM, C.S., HOWES, G. G., SUNDKVIST, D., BALE, S. D., CHASTON, C. C., CHEN, C. H. K. & MOZER, F. S. 2012 Identification of kinetic Alfvén wave turbulence in the solar wind. *Astrophys. J. Lett*. **745** (1), L9.

SERVIDIO, S., CHASAPIS, A., MATTHAEUS, W. H., PERRONE, D., VALENTINI, F., PARASHAR, T. N., VELTRI, P., GERSHMAN, D., RUSSELL, C. T., GILES, B., *et al.* 2017 Magnetospheric multiscale observation of plasma velocity-space cascade: hermite representation and theory. *Phys. Rev. Lett*. **119** (20), 205101.

SERVIDIO, S., DMITRUK, P. A., GRECO, A., WAN, M., DONATO, S., CASSAK, P. A., SHAY, M. A., CARBONE, V. & MATTHAEUS, W. H. 2011 Magnetic reconnection as an element of turbulence. *Nonlinear Process. Geophys*. **18** (5), 675.

SERVIDIO, S., MATTHAEUS, W. H. & DMITRUK, P. 2008 Depression of nonlinearity in decaying isotropic MHD turbulence. *Phys. Rev. Lett*. **100** (9), 095005.

SERVIDIO, S., MATTHAEUS, W. H., SHAY, M. A., CASSAK, P. A. & DMITRUK, P. 2009 Magnetic reconnection in two-dimensional magnetohydrodynamic turbulence. *Phys. Rev. Lett*. **102** (11), 115003.

SERVIDIO, S., VALENTINI, F., CALIFANO, F. & VELTRI, P. 2012 Local kinetic effects in two-dimensional plasma turbulence. *Phys. Rev. Lett*. **108** (4), 045001.

SERVIDIO, S., VALENTINI, F., PERRONE, D., GRECO, A., CALIFANO, F., MATTHAEUS, W. H. & VELTRI, P. 2015 A kinetic model of plasma turbulence. *J. Plasma Phys*. **81** (1), 325810107.

SETTINO, A., MALARA, F., PEZZI, O., ONOFRI, M., PERRONE, D. & VALENTINI, F. 2020 Kelvin–Helmholtz instability at proton scales with an exact kinetic equilibrium. *Astrophys. J.* **901** (1), 17.

SMITH, C. W., MATTHAEUS, W. H., ZANK, G. P., NESS, N. F., OUGHTON, S. & RICHARDSON, J. D. 2001 Heating of the low-latitude solar wind by dissipation of turbulent magnetic fluctuations. *J. Geophys. Res*. **106** (A5), 8253–8272.

SORRISO-VALVO, L., CARBONE, V., NOULLEZ, A., POLITANO, H., POUQUET, A. & VELTRI, P. 2002 Analysis of cancellation exponents in two-dimensional MHD turbulence. *Phys. Plasmas* **9**, 89.

SORRISO-VALVO, L., CARBONE, V., VELTRI, P., CONSOLINI, G. & BRUNO, R. 1999 Intermittency in the solar wind turbulence through probability distribution functions of fluctuations. *Geophys. Res. Lett*. **26** (13), 1801–1804.

SORRISO-VALVO, L., CATAPANO, F., RETINÒ, A., LE CONTEL, O., PERRONE, D., ROBERTS, O. W., COBURN, J. T., PANEBIANCO, V., VALENTINI, F., PERRI, S., *et al.* 2019 Turbulence-driven ion beams in the magnetospheric Kelvin–Helmholtz instability. *Phys. Rev. Lett*. **122** (3), 035102.

SORRISO-VALVO, L., MARINO, R., CARBONE, V., NOULLEZ, A., LEPRETI, F., VELTRI, P., BRUNO, R., BAVASSANO, B. & PIETROPAOLO, E. 2007 Observation of inertial energy cascade in interplanetary space plasma. *Phys. Rev. Lett*. **99**, 115001.

SORRISO-VALVO, L., PERRONE, D., PEZZI, O., VALENTINI, F., SERVIDIO, S., ZOUGANELIS, I. & VELTRI, P. 2018 Local energy transfer rate and kinetic processes: the fate of turbulent energy in two-dimensional hybrid Vlasov–Maxwell numerical simulations. *J. Plasma Phys*. **84** (2), 725840201.

SULEM, P. L. & PASSOT, T. 2015 Landau fluid closures with nonlinear large-scale finite Larmor radius corrections for collisionless plasmas. *J. Plasma Phys*. **81** (1), 325810103.

TENBARGE, J. M. & HOWES, G. G. 2012 Evidence of critical balance in kinetic Alfvén wave turbulence simulations. *Phys. Plasmas* **19** (5), 055901.

TENBARGE, J. M. & HOWES, G. G. 2013 Current sheets and collisionless damping in kinetic plasma turbulence. *Astrophys. J. Lett*. **771** (2), L27.

TU, C.-Y. & MARSCH, E. 1995 MHD structures, waves and turbulence in the solar wind: observations and theories. *Space Sci. Rev*. **73** (1–2), 1–210.

VAIVADS, A., RETINÒ, A., SOUCEK, J., KHOTYAINTSEV, Y. V., VALENTINI, F., ESCOUBET, C. P., ALEXANDROVA, O., ANDRÉ, M., BALE, S. D., BALIKHIN, M., *et al.* 2016 Turbulence heating observer–satellite mission proposal. *J. Plasma Phys*. **82** (5), 905820501.

VALENTINI, F., PERRONE, D., STABILE, S., PEZZI, O., SERVIDIO, S., DE MARCO, R., MARCUCCI, F., BRUNO, R., LAVRAUD, B., DE KEYSER, J., *et al.* 2016 Differential kinetic dynamics and heating of ions in the turbulent solar wind. *New J. Phys*. **18** (12), 125001.

VALENTINI, F., PERRONE, D. & VELTRI, P. 2011 Short-wavelength electrostatic fluctuations in the solar wind. *Astrophys. J*. **739** (1), 54.

VALENTINI, F., TRÁVNÍČEK, P., CALIFANO, F., HELLINGER, P. & MANGENEY, A. 2007 A hybrid-Vlasov model based on the current advance method for the simulation of collisionless magnetized plasma. *J. Comput. Phys*. **225** (1), 753–770.

VALENTINI, F., VÁSCONEZ, C. L., PEZZI, O., SERVIDIO, S., MALARA, F. & PUCCI, F. 2017 Transition to kinetic turbulence at proton scales driven by large-amplitude kinetic Alfvén fluctuations. *Astron. Astrophys*. **599**, A8.

VALENTINI, F., VELTRI, P., CALIFANO, F. & MANGENEY, A. 2008 Cross-scale effects in solar-wind turbulence. *Phys. Rev. Lett*. **101** (2), 025006.

VAN LEER, B. 1977 Towards the ultimate conservative difference scheme. III. Upstream-centered finite-difference schemes for ideal compressible flow. *J. Comput. Phys*. **23** (3), 263–275.

VÁSCONEZ, C. L., PUCCI, F., VALENTINI, F., SERVIDIO, S., MATTHAEUS, W. H. & MALARA, F. 2015 Kinetic Alfvén wave generation by large-scale phase mixing. *Astrophys. J*. **815** (1), 7.

VÁSCONEZ, C. L., VALENTINI, F., CAMPOREALE, E. & VELTRI, P. 2014 Vlasov simulations of kinetic Alfvén waves at proton kinetic scales. *Phys. Plasmas* **21** (11), 112107.

VERDINI, A., GRAPPIN, R., HELLINGER, P., LANDI, S. & MÜLLER, W. C. 2015 Anisotropy of the third-order structure functions in MHD turbulence. *Astrophys. J.* **804** (2), 119.

WAN, M., MATTHAEUS, W. H., ROYTERSHTEYN, V., KARIMABADI, H., PARASHAR, T., WU, P. & SHAY, M. 2015 Intermittent dissipation and heating in 3D kinetic plasma turbulence. *Phys. Rev. Lett*. **114** (17), 175002.

WU, P., PERRI, S., OSMAN, K., WAN, M., MATTHAEUS, W. H., SHAY, M. A., GOLDSTEIN, M. L., KARIMABADI, H. & CHAPMAN, S. 2013 Intermittent heating in solar wind and kinetic simulations. *Astrophys. J. Lett*. **763** (2), L30.

YANG, Y., MATTHAEUS, W. H., PARASHAR, T. N., WU, P., WAN, M., SHI, Y., CHEN, S., ROYTERSHTEYN, V. & DAUGHTON, W. 2017 Energy transfer channels and turbulence cascade in Vlasov–Maxwell turbulence. *Phys. Rev.* E **95** (6), 061201.

ZIMBARDO, G., GRECO, A., SORRISO-VALVO, L., PERRI, S., VÖRÖS, Z., ABURJANIA, G., CHARGAZIA, K. & ALEXANDROVA, O. 2010 Magnetic turbulence in the geospace environment. *Space Sci. Rev*. **156** (1–4), 89–134.